Regulating d-Band Center of Ti2C MXene Via Nb Alloying for Stable and High-Efficient Supercapacitive Performances

Guan, Yunfeng; Cong, Ye; Zhao, Rong; Li, Ke; Li, Xuanke; Zhu , Hui; Zhang, Qin; Dong, Zhijun & YANG, Nianjun (2023) Regulating d-Band Center of Ti2C MXene Via Nb Alloying for Stable and High-Efficient Supercapacitive Performances. In: Small, 19 (35) (Art N° 2301276).

DOI: 10.1002/smll.202301276
Handle: http://hdl.handle.net/1942/40140

Regulating *d*-band center of Ti_2C MXene via Nb alloying for stable and high-efficient supercapacitive performances

Yunfeng Guan, Ye Cong, Rong Zhao, Ke Li, Xuanke Li, Hui Zhu, Qin Zhang, Zhijun Dong, Nianjun Yang**

Y. Guan, Y. Cong, R. Zhao, X. Li, H. Zhu, Q. Zhang, Z. Dong
Hubei Province Key Laboratory of Coal Conversion and New Carbon Materials, School of Chemistry and Chemical Engineering
Wuhan University of Science and Technology
Wuhan 430081, China
E-mail: congye@wust.edu.cn
K. Li
School of Chemistry, Centre for Research on Adaptive Nanostructures and Nanodevices (CRANN) & Advanced Materials and Bio-Engineering Research (AMBER) Centre
Trinity College Dublin, Dublin, Dublin 2, Ireland
N. Yang
Institute of Materials Engineering, University of Siegen, 57076 Siegen, Germany
Department of Chemistry, Hasselt University, Agoralaan 1 - Buidling D, 3590 Diepenbeek, Belgium
IMO-IMOMEC, Hasselt University, Wetenschapspark 1, 3590 Diepenbeek, Belgium
E-mail: nianjun.yang@uhasselt.be

Keywords: Ti_2C MXene, alloy engineering strategy, stability, DFT calculation, supercapacitor

Ti_2C MXene with the lowest formula weight is expected to gain superior advantages in gravimetric capacitances over other heavier MXenes. Nevertheless, its poor chemical and electrochemical stability is the most fatal drawback and seriously hinders its practical applications. Herein, we propose an alloy engineering strategy at the M-sites of Ti_2C MXene. Theoretical calculations reveal that the electronic redistribution of the solid-solution TiNbC MXene improves the electronic conductivity, induces the upward *d*-band center, tailors the surface functional groups, and increases the electron loss impedance, resulting in its excellent capacitive performance and high chemical stability. The as-prepared flexible TiNbC film delivers specific capacitance up to 381 F g^{-1} at a scan rate of 2 mV s^{-1} and excellent electrochemical stability without capacitance loss after 10000 charge/discharging cycles. This

work provides a universal approach to develop high-performance and chemically stable MXene electrodes.

1. Introduction

Supercapacitors (SCs) have attracted great attention in both academic and industrial communities, owing to their high power densities, long lifespan and ultrafast charge/discharge rate[1–3]. Among various SC components, the capacitor electrode is regarded as one of the most crucial aspects that determines the overall electrochemical performance of a SC. Conventional electrical double-layer capacitors based on carbon materials mainly store energy through physical ion adsorption/desorption, which inevitably encounters low energy density due to the limited specific surface area[4]. The pseudocapacitive materials (e.g., metal oxide and conducting polymers) are promising alternatives to double-layer capacitive materials accounting for the fast surface redox reactions[5]. However, they always exhibit poor electronic conductivity and structural stability. Consequently, exploring high-performance SC electrodes is the focal spot and feasible approach to boost the further SC development.

MXene materials, a family of two-dimensional early transition metal carbides, nitrides and carbonitrides, have shown superior electrochemical properties in the field of energy storage. This is due to their excellent electrical conductivities, good hydrophilicity, controllable layer spacing and rich surface function groups[2,6,7]. They can easily synthesized by selectively extracting the A atom layer from layered $M_{n+1}AX_n$ phase (n = 1, 2, 3, 4) in fluoride-containing solutions or molten salts[8,9], where M stands for a transition metal (e.g., Sc, Ti, V, Cr, Nb, Mo, etc.), A refers to an element from the IIIA or IVA group (e.g., Al, Si, Ga, etc.), and X represents C, N or CN. Among numerous MXenes, Ti_3C_2 is the most widely studied, due to its great overall performance. On the other hand, theoretical calculations have predicted that M_2X MXenes (e.g., Ti_2C, Nb_2C, and V_2C) can show higher gravimetric capacitances than M_3X_2 MXenes (e.g., Ti_3C_2) and M_4X_3 MXenes (e.g., V_4C_3). This is because their molecular weights are lower, but their specific surface area are higher and their abundant active sites are more[10]. Clearly, Ti_2C MXene has the lowest formula weight and thus tends to possess the highest gravimetric capacitance[10]. Unfortunately, Ti_2C suffers from poor chemical and electrochemical stability caused by highly reactive chemical surface chemistry[11], which in turn results in the formation of bonds between the exposed transition metal and oxygen[12]. The gradual oxidation or dissolution of titanium in aqueous sulfuric acid electrolyte during energy storage process therefore leads to a sharp decline in cycling performance[13].

It is known that alloy engineering, namely the introduction of external transition metal atoms into M-site of MXenes, is an effective strategy to regulate the physical and chemical properties of original MXenes since such MXene alloys can vary compositions, surface function groups, electronic structure, and lattice structures of MXenes[14,15]. For example, the reported Mo_2TiC_2 and $(V_{1-x}Ti_x)_2C$ MXenes have exhibited higher Coulombic efficiencies and electrochemical performance than their corresponding mono-M element MXenes[16,17]. Notably, a niobium (Nb) atom with partially filled orbitals ($4d^45s^1$) is expected to be one of the best alloy elements since it tends to achieve good bonding with other metals and is thus favourable for fusing the merits of different components. Nb-based MXenes have shown better stability in comparison to Ti_2C MXenes[18,19], where similar atomic radius of Nb and Ti atoms are favourable for mutual lattice substitution between transition metal Ti and Nb atoms. Therefore, the introduction of Nb at the M sites of Ti_2C is believed to improve chemical stability of Ti_2C and further to promote its SC performance. Surprisingly, the intrinsic effects of an alloying approach on Ti_2C MXene have not been well revealed up to date.

Herein, we employ an alloy engineering strategy to synthesize flexible TiNbC films, clarify the stability improvement by means of theoretical and experimental approaches, and further utilize as the capacitor electrode in acidic media to construct high-performance SC devices. The as-synthesized flexible TiNbC film shows significant improvement in chemical stability and electrochemical properties in comparison to Ti_2C. Systematic experiments and theoretical calculations reveal the intrinsic effects of Nb substitution on the electronic structure, surface chemistry, stability behaviour and electrochemical performance. Density functional theory (DFT) calculations indicate that the introduction of Nb atoms improves the electronic conductivity, induces the upshifted *d*-band centre, tailors the surface functional groups, and increases the electron loss impedance, promoting its electrochemical performance and its chemical stability.

2. Results and Discussion

2.1 DFT calculations of surface chemistry and electronic structure of MXenes

Ti_2C MXene is known to feature good electrochemical performance. However, it suffers from poor chemical and electrochemical stability, caused by its high chemical reactivity. In turn, this leads to a sharp decline in its cycling performance when Ti_2C MXene is employed as a capacitor electrode in an acidic electrolyte solution. A reasonable strategy is to form alloyed MXene since its electronic structure can be regulated, probably leading to its improved chemical and electrochemical stability. Prior to proving such an assumption through experiments, the surface

chemistry, electronic structure, and work function before and after alloying were investigated by means of density functional theory (DFT). It is well acknowledged that the nature of MXene such as hydrophilicity and chemical stability is closely related to the surface functional groups. Among various functional groups, the oxygen-containing terminations play an important role in the stability of Ti_2C MXenes[20]. Since the valence state of transition metal on oxygen-terminated MXene is higher than that on fluorinated MXene, oxygen-terminated MXenes are expected to feature better stability than fluorinated MXenes. In this regards, TiNbC MXene models were optimized with different functional groups/terminations such as -OH (**Figure 1a**), -O (**Figure 1b**), -F (**Figure 1c**) and -Cl (**Figure 1d**) at various possible sites. Other possible simulation models of TiNbC MXenes that are functionalized with -OH (**Figure S1a-c**), -O (**Figure S2a-c**), -F (**Figure S3a-c**) and -Cl (**Figure S4a-c**) at other different sites were also proposed. To check their structural stability, the corresponding cohesive energies were systematically investigated by DFT calculations. The cohesive energy per atom ($E_{coh/atom}$) was evaluated according to the following equation[21]:

$$E_{coh/atom} = [E_{tot}(NbTiCT_x - E_{atom}(Ti) - E_{atom}(Nb) - E_{atom}(C) - 2E_{atom}\ (O/H/F/Cl)/n, \quad (1)$$

where n refers to the number of atoms, E_{tot} stands for the total energy of $TiNbCT_x$, and E_{atom} represents the individual atoms energy. From the calculated $E_{coh/atom}$ values of TiNbC MXene with various groups at different sites (**Figure 1e**, **Figure S1d**, **Figure S2d**, **Figure S3d** and **Figure S4d**), one can find that the calculated $E_{coh/atom}$ values for those with the same terminations are essentially same even when these terminations are at different sites. In other words, the sites of such terminations have minor effect on the ultimate $E_{coh/atom}$ values. The comparison of $E_{coh/atom}$ values reveals that TiNbC MXenes with oxygen-containing terminations have the highest structural stability.

The adsorption energies, E_{ads}, of such functional groups were further evaluated since they are informative to predict the preferred functional groups on the MXene surface. The adsorption energies of MXenes with various functional groups at different sites were calculated using the equation of[22]:

$$E_{ads} = \left[E_{tot(NbTi\ \ _2)} - \left(E_{NbTiC} + E_{T_2}\right)\right]/2, \quad (2)$$

where $E_{tot(NbTi\ \ _2)}$ is the total energy of functionalized MXenes, E_{NbTiC} and E_{T_2} are the energies of pure TiNbC MXene and the isolated functional groups, respectively. From the calculated E_{ads} values for various functional groups at different sites (**Figure 1f**, **Figure S1e**, **Figure S2e**, **Figure S3e**, and **Figure S4e**), TiNbC MXenes with oxygen functional groups (-OH and -O) have stronger adsorption ability than those with other functional groups. Therefore,

the calculated results prove that TiNbC MXene is preferred with oxygen-containing functional groups and tends to possess good chemical stability.

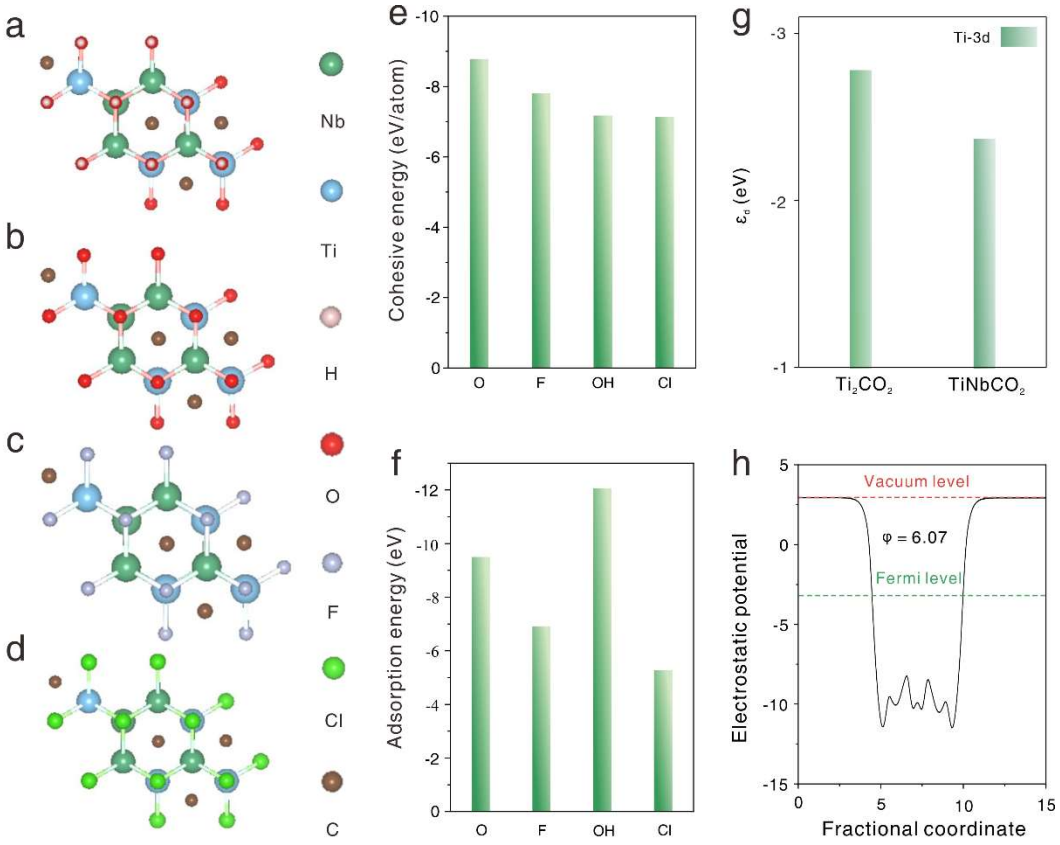

Figure 1. Optimal simulation models of TiNbC MXene with various functional groups for (a) -OH, (b) -O, (c) -F and (d) -Cl. Calculated (e) cohesive energies and (f) adsorption energies for different functionalized TiNbC MXenes. (g) *d*-band center evolutions of Ti_2CO_2 and $TiNbCO_2$. (h) The calculated work functions of TiNbC MXene.

The evolution of surface chemistry of *f*-TiNbC film was further theoretically revealed. Namely, the electron structures before and after Nb alloying were investigated by means of the DFT method. Related models were simulated and their density of states (DOSs) before and after alloying Nb were calculated (**Figure S5**). The density of states of $TiNbCO_2$ at Fermi level are mainly donated by Nb-d and Ti-d orbitals. The electronic structure and surface chemistry properties of $TiNbCO_2$ are thus controlled by both Nb and Ti layers. Since the *d*-band center can be used to evaluate the chemical affinity and adsorption performance of the adsorbent[23], the *d*-band center of the MXene before and after alloying with Nb was calculated. The calculated results (**Figure 1g**) reveal that the *d*-band center is closer to the Fermi level after its alloying with Nb, indicating the enhanced chemical affinity and adsorption capability toward oxygen-containing functional groups. From the calculated work function values of Ti_2C MXene

before and after the application of this alloying process, it is obvious that TiNbC MXene (**Figure 1h**) has higher work functions in comparison to Ti_2C MXene (**Figure S6**). The increase of these work functions results in significant reduction of electron loss, thereby enhancing its chemical stability[24,25]. Therefore, the proposed alloying strategy may be an effective way to improve the chemical and electrochemical stability of Ti_2C MXene.

2.2 Synthesis and characterization of MXenes

Prior to verify the theoretical predictions, our TiNbC MXenes were prepared *via* selective etching of TiNbAlC with a solution of lithium fluoride and hydrochloric acid (**Figure 2a**). The obtained sample was repeatedly washed with alcohol and deionized water until the pH of the supernatant approached to 7. Subsequently, the mixture was redispersed and sonicated in a tetramethylammonium hydroxide (TMAOH) solution. The black supernatant was collected and used for further experiments.

To check such a synthesis process, the X-ray diffraction (XRD) patterns of the TiNbAlC, Ti_2AlC, and Nb_2AlC MAX phases were recorded (**Figure 2b**). As confirmed by their XRD patterns, as-prepared MAX phases are highly pure. Notably, there are no obvious branching peaks in the XRD patterns of TiNbAlC, indicating the uniform distribution of various elemental species[14]. Related characteristic regions were magnified and displayed in green (**Figure 2c**), purple (**Figure 2d**), and pink (**Figure 2e**) domains. The introduction of Nb into Ti_2AlC MAX leads to the shift of all peaks to lower angles, suggesting an increase of the *c* lattice constant and an expansion of layer spacings. Conversely, when Ti atoms are introduced into the Nb_2AlC MAX phase, its (002) peak shifts to a higher angle, which is caused by lattice shrinkage. This is ascribed to larger atomic radius of Nb species (164 pm) as compared to Ti species (160 pm), leading to a lattice mismatch and deviation in the TiNbAlC MAX phase[26]. This is further proved by the scanning electron microscopy (SEM) image of TiNbAlC MAX phase (**Figure 2f**), where a dense and layered structure is noticed, similar to those of Ti_2AlC (**Figure S7**) and Nb_2AlC (**Figure S8**). In addition, the elements of Nb, Ti, Al, and C are uniform distributed in TiNbAlC MAX phase, as proved by its EDS mapping (**Figure 2g**).

In the SEM image of TiNbC MXene (**Figure 3a**), an accordion-like structure is clearly visible. From related energy dispersive spectroscopy (EDS) spectra (**Figure S9**), homogeneous dispersion of Ti, Nb, O, and C elements is confirmed. Moreover, the TiNbC suspension reveals obvious Tindal effect (**Figure 3b**), similar to the Ti_2C (**Figure S13**) and Nb_2C (**Figure S14**) suspensions. Stacked nanosheets of as-formed films using such suspensions are also clearly observed. From the comparison of the XRD patterns of TiNbAlC MAX phase with those of

TiNbC film (**Figure 3c**), it is observed the diffraction peaks of TiNbAlC disappear completely after the etching and delamination processes due to the successful removal of Al layers. A new peak appears at $2\theta \approx 7.22^{o}$. It can be assigned to the (002) characteristic peak of TiNbC MXene, corresponding to a larger layer spacing of 12.1 Å in comparison to the precursor (6.8 Å).

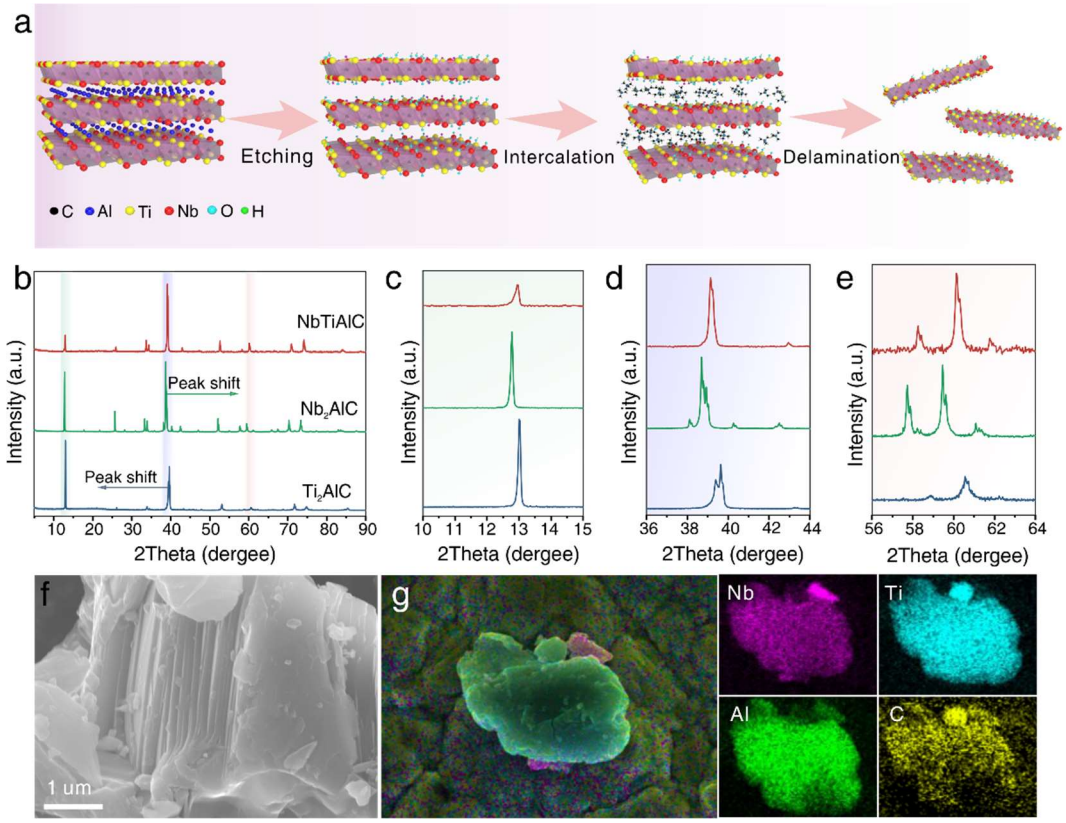

Figure 2. (a) Schematic diagram of preparation and delamination of TiNbC MXene. (b) XRD patterns of as-prepared TiNbAlC, Ti_2AlC and Nb_2AlC MAX phases. (c-e) Amplified diffraction patterns of (b). (f) SEM image of a TiNbAlC MAX phase and (g) its EDS element mapping.

Based on the results of XPS spectra (**Figure 3d**), the fluorine content in the *f*-TiNbC MXene is the lowest and the oxygen content is highest (**Table S1**), resulting in reduced diffusion barrier and improved reaction kinetics[27]. The high resolution XPS spectra of C 1s (**Figure. 3e**) exhibit two strong peaks located at 283.5 and 284.3 eV, which are attributed to C-Ti/C-Nb and C-C in TiNbC MXene[28]. Moreover, three weak characteristic peaks located at 285.2 eV, 285.8 eV and 288.3 eV can be attributed to C-H, C-O and O-C=O, respectively, indicating the successful preparation of TiNbC MXene. Its high resolution XPS spectra of O 1s (**Figure 3f**) have been fitted into three components. They are located at about 529.9, 530.9, and 532.1 eV, corresponding to oxygen-containing functional groups generated during an exfoliation process[29]. After the introduction of Nb species into Ti_2C, the O 1s XPS peaks shift clearly to the locations with higher binding energies, implying strong interactions between oxygen-

containing terminations and transition metals. Moreover, the atomic percentage of -O groups is significantly higher than that of -OH groups, consistent well with the theoretical calculation result. Such favourable surface chemistry further supports well the improved stability of *f*-TiNbC film, as predicted from DFT calculations.

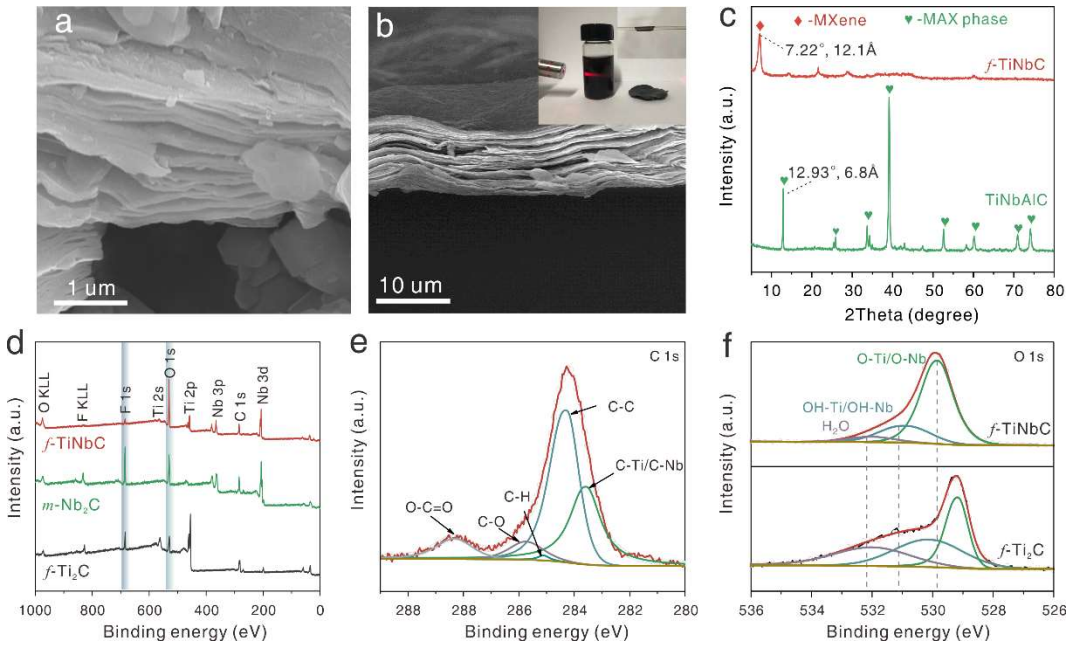

Figure 3. (a) SEM image of TiNbC MXene. (b) Cross-section SEM image of TiNbC film (insert: Optical image of the flexible TiNbC film and its Tindall effect). (c) XRD patterns of the fresh TiNbC film. (d) XPS survey spectra of *f*-Ti_2C, *m*-Nb_2C and *f*-TiNbC. High-resolution XPS spectra of C 1s (e) and O 1s (f) of *f*-TiNbC.

2.3 Chemical stability of MXenes

To verify the theoretical prediction, the chemical stability of this alloyed MXene was investigated. The characteristic MXene peak (**Figure 4a**) of as-synthesized *m*-Ti_2C disappears completely after its exposure to air at room temperature for 60 days. Such a stored sample exhibits a damaged accordion-like layered structure (**Figure S15**), indicating an poor chemical stability. However, for stored *m*-TiNbC MXenes under identified conditions, both their (002) MXene peak (**Figure 4b**) and two-dimensional structure (**Figure 4c**) are well preserved. This characteristic peak slightly shifts to right, attributed to the loss of water molecules between MXene layers. The improved chemical stability may be attributed to the higher work function (**Figure 1h**) in comparison to Ti_2C MXene (**Figure S6**), resulting in significantly lower electron losses. Therefore, the proposed alloying strategy may be an effective way to improve its chemical stability.

The stability of MXene film was tested to further demonstrate the feasibility of this alloy

strategy. As expected, the *f*-Ti_2C film (**Figure 4d**) exhibits poor chemical stability. It loses its mechanical robustness and breaks after storage in air at room temperature for 12 h. This stems from its oxidization in air, as confirmed from the comparison of the XPS spectra of *f*-Ti_2C film before (**Figure S16**) and after (**Figure S17**) its storage in air, where distinct titanium dioxide (TiO_2) peaks are clearly presented. In contrast, the *f*-TiNbC film displays good flexibility after its oxidation in air for 48 h (**Figure 4e**). Moreover, no clear variation in XRD patterns (**Figure 4f**) and XPS spectra (**Figure 4g**) has been found. The fitted Ti-O peaks in the XPS spectra of the fresh *f*-TiNbC film are attributed to the surface oxygen-containing terminations[13].

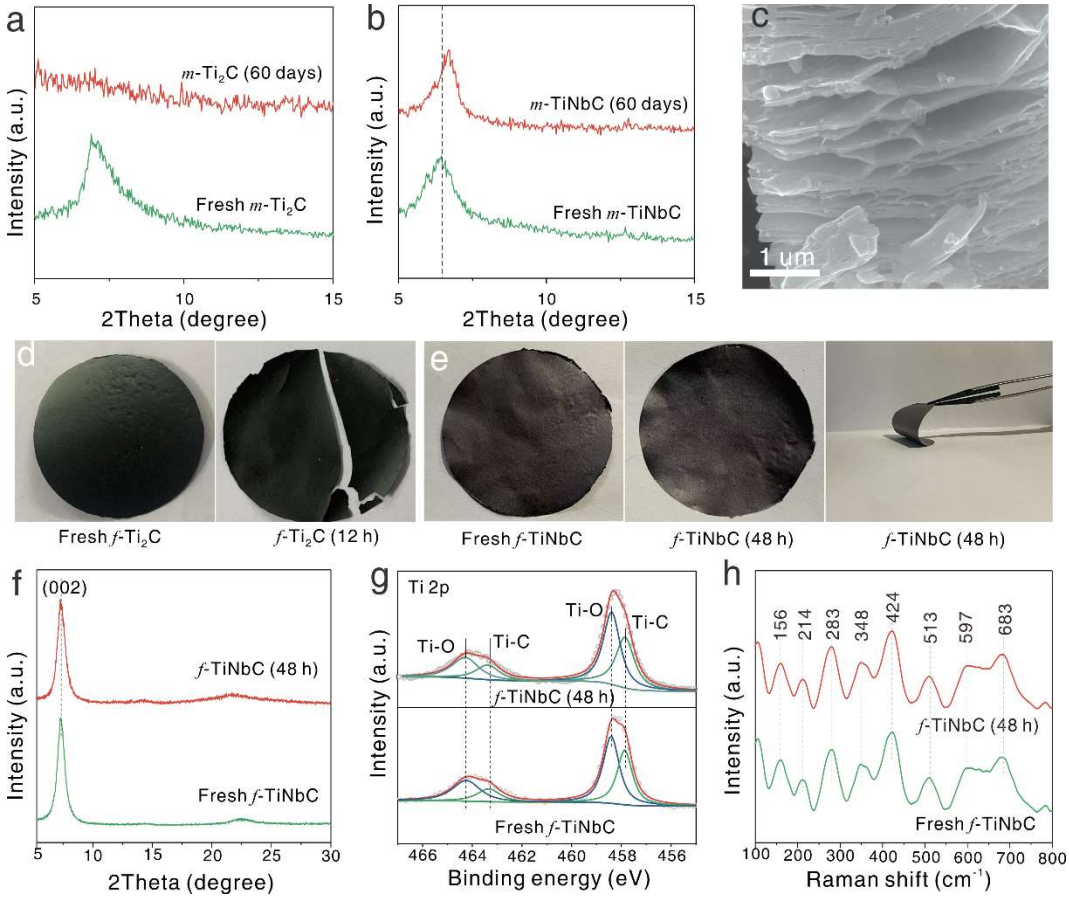

Figure 4. XRD patterns of (a) *m*-Ti_2C, (b) *m*-TiNbC and (c) SEM image of *m*-TiNbC after its oxidation in air at room temperature. Digital photographs of the *f*-Ti_2C (d) and *f*-TiNbC (e) films before and after their oxidation in air at room temperature. (f) XRD patterns of *f*-TiNbC MXene before and after its storage in air for 48 h. (g) High-resolution Ti 2p XPS spectrum and (h) Raman spectrum of the *f*-TiNbC film before and after its oxidation for 48 h.

In the Raman spectrum of the TiNbC MXene (**Figure 4h**), the peaks located at 156, 214, 283, 424 and 597 cm^{-1} can be ascribed to the E_{2g}, E_{1g}, E_{1g}, A_{1g} and E_{2g} Raman active modes, respectively[13,30,31]. There are no visible vibration peaks of anatase TiO_2[32,33] in the Raman spectra of the *f*-TiNbC before and after its storage in air for 48 h . All these results verify the

significantly improved chemical stability of the *f*-Ti_2C film via the alloy strategy.

2.4 Electrochemical behaviour and stability

To further investigate the electrochemical stability, the electrochemical performances of MXene before and after alloying Nb were measured. To get more details about the capacitive behaviour of the TiNbC electrode, the CVs were recorded at different scan rates (**Figure 5a**). A pair of broad peaks are visible, indicating the pseudocapacitive reactions dominate electrochemical energy storage process of this electrode. Notably, a similar curvilinear shape is still preserved even at scan rates up to 100 mV s^{-1}, implying its outstanding rate performance. The CV curve of *f*-TiNbC shows the largest area (**Figure 5b**) at 2 mV s^{-1} in 3 M H_2SO_4, indicating its highest specific capacitance compared with single metal carbide MXenes (Ti_2C and Nb_2C). The variation of related peak currents was studied as a function of scan rates (**Figure 5c**). To estimate the contribution of such pseudocapacitive capacitance into the total capacitive capacitance, the *b* values for the TiNbC MXene electrode at different scan rates were calculated[13]. They are 0.87 and 0.79 for oxidation and reduction peaks, respectively. Since these values are close to 1, the pseudocapacitance contribution is predominant for the total capacitance of the TiNbC electrode. In addition, its pseudocapacitance contribution increases gradually when scan rate increases from 2 mV s^{-1} to 100 mV s^{-1} (**Figure 5d**). It reaches to 71.4% at a scan rate of 100 mV s^{-1}.

The specific capacitances of TiNbC, Ti_2C and Nb_2C electrodes were evaluated (**Figure 5e**) at various scan rates. At a scan rate of 2 mV s^{-1}, the maximum specific capacitances of the TiNbC, Ti_2C and Nb_2C electrodes are 381, 281, and 115 F g^{-1}, respectively. Moreover, at other scan rates, the TiNbC film still delivers the highest specific capacitance compared to Ti_2C and Nb_2C electrodes. This is due to its faster ion transport of the aqueous electrolyte, owing to its lower fluorine-content and higher amount of oxygen-containing functional groups. The *f*-TiNbC MXene electrode shows a poor rate performance in comparison to the *f*-Ti_2C MXene electrode, probably due to its smaller average layer spacing (**Table S2**). In more detail, its larger molecular weight might reduce its layer spacing during the vacuum filtration process. The GCD curves of the TiNbC electrode were also recorded at different current densities (**Figure 5f**). They have similar triangular shape at the current densities varied from 1 to 10 A g^{-1}, proving good reversibility of this TiNbC electrode. At the same current density, the TiNbC electrode presents the longer discharge time (**Figure 5g**) in comparison to the Ti_2C MXene (**Figure S18**) and Nb_2C MXene (**Figure S19**). This corresponds to its higher specific capacitance, as testified in their CVs.

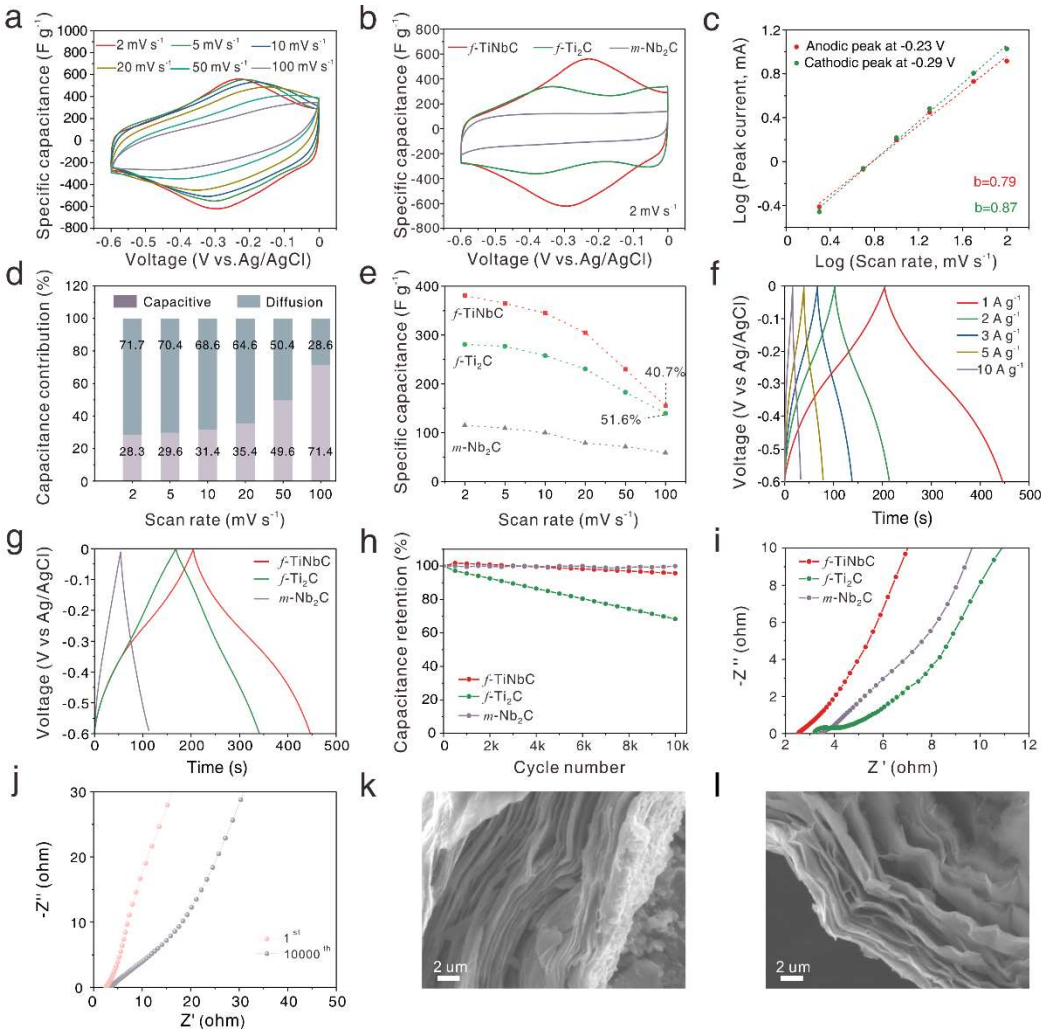

Figure 5. Electrochemical properties of MXene electrodes for the supercapacitor construction. (a) CVs of the *f*-TiNbC electrode at different scan rates. (b) CVs of different MXene electrodes at 2 mV s^{-1} in 3 M H_2SO_4. (c) The variation of the peak currents as a function of scan rates. (d) Capacitive contribution of the TiNbC MXene electrodes into their total capacitances at different scan rates. (e) Comparison of the specific capacitances of the *m*-Nb_2C, *f*-TiNbC and *f*-Ti_2C electrodes at various scan rates. (f) GCD curves of the *f*-TiNbC electrode at various current densities in 3 M H_2SO_4. (g) Comparison of the GCD curves of the *m*-Nb_2C, *f*-TiNbC and *f*-Ti_2C electrodes at a current density of 1 A g^{-1}. (h) Capacitance retention of the *m*-Nb_2C, *f*-TiNbC and *f*-Ti_2C electrodes at a current density of 10 A g^{-1}. (i) Nyquist curves of different MXene electrodes. (j) Nyquist plots of the 1st and 10000th cycles for the TiNbC MXene film at a current density of 10 A g^{-1} in 3 M H_2SO_4. (k, l) SEM images of the TiNbC MXene film before and after 10000 cycling at a current density of 10 A g^{-1}.

The electrochemical stability of these MXene electrodes were tested at a current density of 10 A g^{-1} (**Figure 5h**). The capacitance retention of both *f*-TiNbC and *m*-Nb_2C electrodes are

close to 100% even after 10000 GCD cycles, while this value for the *f*-Ti_2C electrode is only about 70%. This remarkable difference can be mainly attributed to the poor antioxidant ability of Ti_2C MXene in H_2SO_4 electrolyte. Namely, the reduction of active substances during the GCD cycling test leads to sharp capacitance attenuation[13].

Moreover, electrochemical impedance spectroscopy (EIS) was employed to evaluate the internal resistance of the TiNbC electrode. The impedance of the as-synthesized flexible TiNbC film (**Figure 5i, Figure S20** and **Table S3**) is small, an indication of its good electron conductivity. The electron transfer at the interface of the film electrode and the electrolyte is expected to be speeded up. To examine the stability of the *f*-TiNbC MXene electrode, its Nyquist plots were recorded before and after 10000 GCD cycles (**Figure 5j**). Only a slight increase in the ohmic resistance (namely from 2.5 ohm to 3.6 ohm) is observed even after 10000 GCD cycles, indicating its good electrochemical stability. In addition, the morphological variation of *f*-TiNbC was analyzed before and after cycling. Its unique two-dimensional layered structure is well preserved before (**Figure 5k**) and after (**Figure 5l**) after long cycling. All these results prove that TiNbC has excellent electrochemical stability.

2.5 Symmetric supercapacitor devices of the TiNbC MXene film

The potential applications in SC of the TiNbC MXene film were tested by assembling a symmetric SC device (**Figure 6a**), where the TiNbC film is used as the working electrode and the electrolyte is 3 M H_2SO_4 aqueous solution. The preservation of curvilinear shape can be clearly observed at various scan rates (**Figure 6b**), indicating its outstanding rate performance. Meanwhile, a similar triangular shape at the current densities varied from 1 to 10 A g^{-1} (**Figure 6c**) demonstrates the good reversibility of this TiNbC electrode. More importantly, electrochemical performance of the TiNbC film greatly exceeds most of reported Ti/Nb-based MXene materials, where the energy/power densities of related devices (**Figure 6d**) and the capacitances (**Figure 6e**) are compared. It delivers maximum energy density of 5.1 mWh g^{-1} at a power density of 350.8 mW g^{-1} and maintains 4.2 mWh g^{-1} at 3617.2 mW g^{-1}.

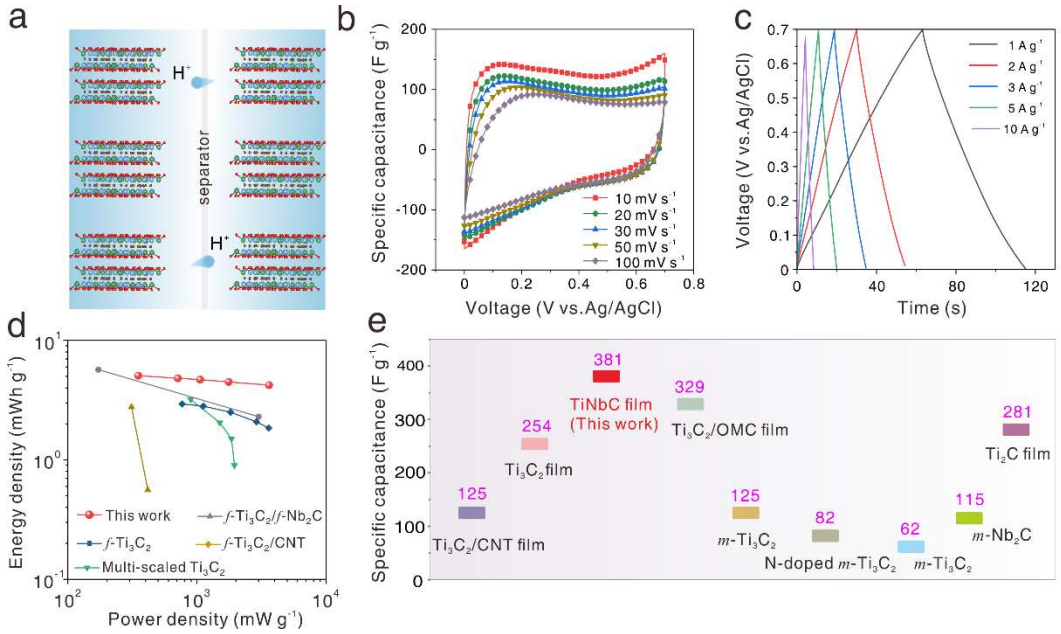

Figure 6. (a) Schematic illustration of the TiNbC film // TiNbC film symmetric supercapacitors device. (b) CVs of *f*-TiNbC based symmetric supercapacitor at various scan rates. (c) The GCD curves of *f*-NbTiC based symmetric supercapacitor at different densities. (d) Ragone plots of *f*-TiNbC and previously reported MXene-based symmetric SCs[34]. (e) Capacitance comparison of different Ti/Nb-based MXene electrodes[35–40].

2.6 Electrochemical mechanism of samples

The intrinsic mechanism of alloying niobium on the enhanced capacitive performance of Ti_2C MXene was further revealed. In this context, its band structures were investigated by first principle DFT calculations. Comparison in the calculated band structures of Ti_2CO_2 (**Figure 7a**), Nb_2CO_2 (**Figure 7b**), and $TiNbCO_2$ (**Figure 7c**), Ti_2CO_2 displays the characteristics of semiconductor, while Nb_2CO_2 is conductor. The alloying of Nb at the M-sites of Ti_2CO_2 probably impairs the structural symmetry and the periodic potential field of Ti_2CO_2, leading to a decrease and split in its energy levels. After alloying niobium at the M-sites of Ti_2CO_2 MXene, it converts from semiconductor to conductor. To prove such a statement, the constant electron densities of Ti_2CO_2 and $TiNbCO_2$ were calculated based on the simulation models (**Figure 7d** and **Figure S21**) and compared (**Figure 7e** and **Figure 7f**). The introduction of niobium leads to a significant increase in electron density. Therefore, the alloying strategy regulates the electron density of state and increases the electron conductivity of MXene, consequently contributing to observable improvements in the electrochemical performance.

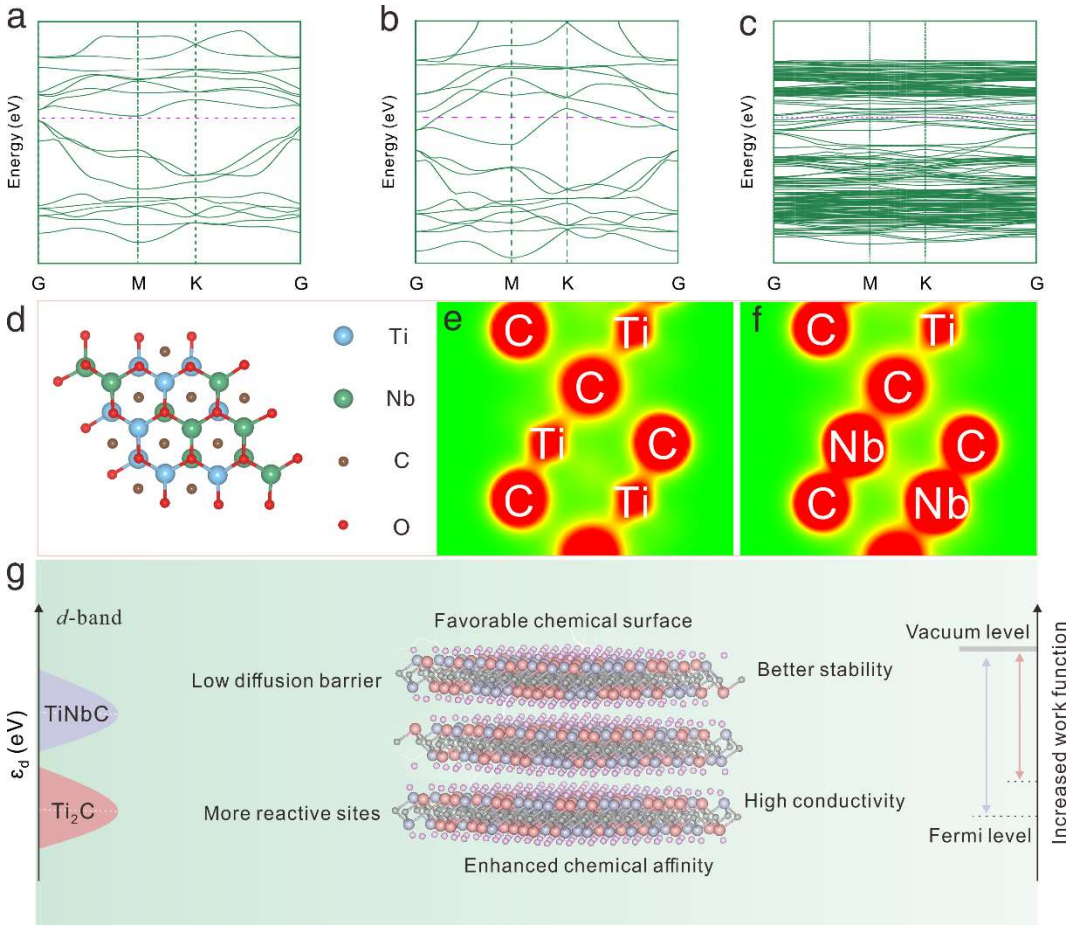

Figure 7. (a-c) Band structures of Ti_2CO_2, Nb_2CO_2 and $TiNbCO_2$, respectively. The Femi level (purple dash line) is set to zero. (d) The simulation model of $TiNbCO_2$. The constant electron densities of Ti_2C before (e) and after (f) alloying Nb, respectively. The red and yellow areas represent the electron density of the corresponding atom. The green area represents the background. (g) Schematic illustration of the advantages after the introduction of Nb into Ti_2C MXene during the energy storage process.

The significant enhancement in stability and electrochemical performance of TiNbC MXene is explained as following (**Figure 7g**). After the alloying of Nb in Ti_2C MXene, the DOSs of $TiNbCO_2$ at Fermi level are mainly donated by the Nb-d and Ti-d orbitals, collectively contributed to the modulation of electronic structure and surface chemistry of Ti_2C MXene. The introduction of Nb species leads to a decrease and split in its energy levels, which increases its electronic conductivity and correspondingly improves the electronic transport. Meanwhile, more electrons are re-located on niobium atoms, which can transfer to the Ti-C bond through the Nb-C bond. In this context, the *d*-band center of the Ti site is closer to the Fermi level. The upshifted *d*-band center induces more reactive reaction sites and thus enhances its chemical affinity and absorbability toward oxygen-containing functional groups, which in turn increases

the content of oxygen-containing functional groups. Eventually, ion diffusion barrier is reduced and reaction kinetics is improved during energy storage. Among various functional groups, the oxygen-containing terminations play important roles in the stability[20]. The valence state of transition metal on an oxygenated MXene is higher than that on fluorinated MXene, due to strong electronic regulation ability, thereby resulting in better stability. Most importantly, the introduction of Nb contributes to higher work function, which leads to great reduction of electron loss, consequently enhancing its environmental stability[24,25]. All these results demonstrate the effectiveness of the alloy strategy in terms of stability and electrochemical properties.

3. Conclusion

In summary, this work systematically investigates the enhancement mechanism of stability and electrochemical property of Ti_2C MXene by means of an alloy strategy. The introduction of Nb into Ti_2C MXene leads to the reduction and splitting of its energy levels, which increases its electronic conductivity and accordingly improves electron transport. Meanwhile, the *d*-band center of Ti is closer to the Fermi level, due to electronic redistribution. Its chemical affinity is enhanced together with its absorbability to oxygen-containing functional groups, thereby tailoring its surface chemistry. Such favourable surface chemistry reduces the ion diffusion barrier, improves the reaction kinetics, and enhances the chemical stability. Moreover, the introduction of niobium into Ti_2C MXene increases the electron loss resistance, thus further improving its chemical stability. The as-synthesized flexible TiNbC MXene film exhibits good chemical stability and excellent capacitive performance. After alloying Nb, the TiNbC MXene film preserves good flexibility after its oxidation in air for 48 h. The maximum specific capacitances of TiNbC at various scan rates are greatly higher than those of Ti_2C and Nb_2C electrodes, delivering 381 F g^{-1}, 281 F g^{-1} and 115 F g^{-1} Nb_2C at 2 mV s^{-1}, respectively. Meanwhile, the electrochemical stability of Ti_2C is visibly improved, and the capacitance retention increases from 77% to nearly 100% after 10,000 cycles at a current density of 10 A g^{-1}. Therefore, this work offers a universal and rational strategy to beneficially regulate chemical stability of MXenes and further promote their applications in the field of energy storage.

4. Experimental Section

Preparation of the MAX phase: The TiNbAlC solid solution MAX precursor was prepared through a simple annealing process[14]. In brief, titanium (Ti), niobium (Nb), aluminum (Al)

and graphite (C) were firstly ball-milled with mass ratio of 1:1:1.1:1 for 24 h. Subsequently, the mixture was transferred into corundum crucible and held at 1500 ºC for 2 h under flowing argon gas. In this way, the TiNbAlC MAX phase was prepared. Similarly, Ti_2AlC and Nb_2AlC MAX phases were prepared, where Nb or Ti were absent in the raw material, respectively.

Preparation and delamination of MXenes: MXenes were prepared by selective etching of the Al layer from layered MAX precursors[14]. First, 1 g TiNbAlC powders were added into a mixed solution of 2 g lithium fluoride and 20 mL hydrochloric acid (12 M). After continuous stirring this mixture at 45 ºC for 48 h, it was washed repeatedly with ethanol, hydrochloric acid, and deionized water. Subsequently, the delamination of TiNbC MXene was carried out by dispersing the obtained multilayer samples into 25 mL of 25 wt.% tetramethylammonium hydroxide (TMAOH) solution. The mixture was stirred for 3 h, further washed with deionized water and separated using ethyl alcohol *via* centrifugation. The TiNbC flexible films were prepared through vacuum filtration of as-obtained suspension. The Ti_2C MXene and Nb_2C MXene were obtained using a similar approach to TiNbC MXene. The multilayer MXene before delamination, delaminated MXene, and the obtained flexible film are labelled throughout the paper as *m*-MXene, *d*-MXene and *f*-MXene, respectively.

Materials characterization: The compositions of samples were assessed by X-ray diffraction using a Cu K*a* radiation. The microstructures and elemental distributions of MXenes were characterized by scanning electron microscope equipped with an energy dispersive spectroscope (SEM, VEGA-3 from TESCAN Inc, China). Raman spectroscopy was performed with laser micro-Raman spectrometer. Chemical compositions of the used samples and their element valence states were analyzed using high-resolution X-ray photoelectron spectroscopy (XPS).

Electrochemical characterization: Electrochemical tests were carried out using a typical three-electrode system in 3 M H_2SO_4 aqueous electrolyte. Activated carbon and Ag/AgCl were used as counter and reference electrodes, respectively. The as-prepared freestanding TiNbC and Ti_2C MXene films with a loading density of about 3 mg cm^{-2} served as the working electrode. To prepare such a film, the Nb_2C MXene powders were firstly mixed with active carbon and polytetrafluoroethylene (PTFE) in ethyl alcohol with weight ratio of 8:1:1. As-obtained slurry was rolled into a flexible film and applied as the working electrode. These electrodes were characterized by means of cyclic voltammetry (CV) at various scan rates (e.g., from 2 to 100 mV s^{-1}) and the galvanostatic charge-discharge (GCD) method at different current densities (e.g., from 1, 2, 3, 5 to 10 A g^{-1}). Electrochemical impedance spectroscopy was performed on CHI 660D electrochemical workstation within the frequency range of 100 mHz to 100 kHz with

an amplitude of 5 mV. The gravimetric specific capacitance (C) of the used electrode was calculated according to[3]:

$$C = \frac{1}{\triangle Vmv}\int idV, \quad (3)$$

where i stands for current, V represents the potential window, v refers to scan rate, and m represents the mass of the used electrode.

The b value can be calculated by[41]:

$$i = av^b, \quad (4)$$

where i stands for peak current, v refers to scan rate, a and b are constants. The capacitive and diffusion-controlled contributions can be evaluated according to[5]:

$$i(V) = k_1 v + k_2 v^{\frac{1}{2}}, \quad (5)$$

where $i(V)$ refers to the current as a function of voltage, v stands for scan rate, $k_1 v$ and $k_2 v^{1/2}$ represent capacitive and diffusion-controlled contributions, respectively.

The energy densities and power densities of a symmetric supercapacitor using *f*-TiNbC MXene were calculated based on previously reported work[34].

DFT calculations: To investigate the energy storage and stability mechanism of the developed MXene electrodes, the first principle density functional theory (DFT) calculations were carried out using the Vienna ab initio Simulation Package (VASP). The exchange–correlation functional was supported by the generalized gradient approximation (GGA) of Perdew–Burke–Ernzernhof (PBE). Structural relaxation stopped until the total energy change was reduced to less than 10^{-6} eV, and the force on each atom was less than 0.01 eV $Å^{-1}$. The sampled Brillouin area was 5 × 5 × 1 in the Monkhorst–Pack grid. The vacuum layer and cut off energy were set to 15 Å and 550 eV, respectively.

Supporting Information

Supporting Information is available from the Wiley Online Library or from the author.

Acknowledgements

This work was supported by the National Natural Science Foundation of China (grant numbers 52002296 and 51902232) and supported by Research Fund of Hubei Provincial Department of Education (Grants Nos. B2019006). The authors gratefully acknowledge the Analytical & Testing Center of Wuhan University of Science and Technology for the help on XPS analysis.

References

[1] M. Ghidiu, M. R. Lukatskaya, M. Q. Zhao, Y. Gogotsi, M. W. Barsoum, *Nature* **2015**, *516*, 78.

[2] A. VahidMohammadi, J. Rosen, Y. Gogotsi, *Science* **2021**, *372*, 1165.

[3] Q. Jiang, Y. Lei, H. Liang, K. Xi, C. Xia, H. N. Alshareef, *Energy Storage Mater.* **2020**, *27*, 78.

[4] D. Feng, T. Lei, M. R. Lukatskaya, J. Park, Z. Huang, M. Lee, L. Shaw, S. Chen, A. A. Yakovenko, A. Kulkarni, J. Xiao, K. Fredrickson, J. B. Tok, X. Zou, Y. Cui, Z. Bao, *Nat. Energy* **2018**, *3*, 30.

[5] K. Li, X. Wang, S. Li, P. Urbankowski, J. Li, Y. Xu, Y. Gogotsi, *Small* **2020**, *16*, 1.

[6] K. Li, M. Liang, H. Wang, X. Wang, Y. Huang, J. Coelho, S. Pinilla, Y. Zhang, F. Qi, V. Nicolosi, Y. Xu, *Adv. Funct. Mater.* **2020**, *30*, 1.

[7] B. Anasori, B. Anasori, M. R. Lukatskaya, Y. Gogotsi, *Nat. Rev. Mater.* **2017**, *2*, 16098.

[8] Y. Guan, S. Jiang, Y. Cong, J. Wang, Z. Dong, Q. Zhang, G. Yuan, Y. Li, X. Li, *2D Mater.* **2020**, *7*, 25010.

[9] M. Li, X. Li, G. Qin, K. Luo, J. Lu, Y. Li, *ACS Nano* **2021***, 15,* 1077-1085.

[10] B. Anasori, M. R. Lukatskaya, Y. Gogotsi, *Nat. Rev. Mater.* **2017**, *2*, 16098.

[11] J. D. Gouveia, F. Viñes, F. Illas, J. R. B. Gomes, *Phys. Rev. Mater.* **2020**, *4*, 1.

[12] M. Naguib, M. Kurtoglu, V. Presser, J. Lu, J. Niu, M. Heon, L. Hultman, Y. Gogotsi, M. W. Barsoum, *Adv. Mater.* **2011**, *23*, 4248.

[13] Y. Guan, R. Zhao, Y. Cong, K. Chen, J. Wu, H. Zhu, Z. Dong, Q. Zhang, G. Yuan, Y. Li, J. Zhang, X. Li, *Chem. Eng. J.* **2021**, *433*, 133582.

[14] M. Han, K. Maleski, C. E. Shuck, Y. Yang, J. T. Glazar, A. C. Foucher, K. Hantanasirisakul, A. Sarycheva, N. C. Frey, S. J. May, V. B. Shenoy, E. A. Stach, Y. Gogotsi, *J. Am. Chem. Soc.* **2020**, *142*, 19110.

[15] Y. Wang, W. Zheng, P. Zhang, W. Tian, J. Chen, Z. M. Sun, *J. Mater. Sci.* **2019**, *54*, 11991.

[16] B. Anasori, Y. Xie, M. Beidaghi, J. Lu, B. C. Hosler, L. Hultman, P. R. C. Kent, Y. Gogotsi, M. W. Barsoum, *ACS Nano* **2015**, *9*, 9507.

[17] M. Naguib, O. Mashtalir, J. Carle, V. Presser, J. Lu, L. Hultman, Y. Gogotsi, M. W. Barsoum, *ACS Nano* **2012**, *6*, 1322.

[18] J. Zhao, J. Wen, J. Xiao, X. Ma, J. Gao, L. Bai, H. Gao, X. Zhang, Z. Zhang, *J. Energy Chem.* **2020**, *53*, 387.

[19] R. B. Rakhi, B. Ahmed, M. N. Hedhili, D. H. Anjum, H. N. Alshareef, *Chem. Mater.* **2015**, *27*, 5314.

[20] N. Xue, X. Li, L. Han, H. Zhu, X. Zhao, J. Zhuang, Z. Gao, X. Tao, *J. Mater. Chem. A* **2022**, *10*, 7960.

[21] S. Yazdanparast, S. Soltanmohammad, A. Fash-White, G. J. Tucker, G. L. Brennecka, *ACS Appl. Mater. Interfaces* **2020**, *12*, 20129.

[22] Y. Xin, Y. X. Yu, *Mater. Des.* **2017**, *130*, 512.

[23] C. Shang, G. Li, B. Wei, J. Wang, R. Gao, Y. Tian, Q. Chen, Y. Zhang, L. Shui, G. Zhou, Y. Hu, Z. Chen, X. Wang, *Adv. Energy Mater.* **2021**, *11*, 1.

[24] H. Zhou, S. J. Han, H. D. Lee, D. Zhang, M. Anayee, S. H. Jo, Y. Gogotsi, T. W. Lee, *Adv. Mater.* **2022**, *41*, 6377.

[25] T. S. Mathis, K. Maleski, A. Goad, A. Sarycheva, M. Anayee, A. C. Foucher, K. Hantanasirisakul, C. E. Shuck, E. A. Stach, Y. Gogotsi, *ACS Nano* **2021**, *15*, 6420.

[26] B. Cordero, V. Gómez, A. E. Platero-Prats, M. Revés, J. Echeverría, E. Cremades, F. Barragán, S. Alvarez, *J. Chem. Soc. Dalt. Trans.* **2008**, *7*, 2832.

[27] Y. M. Li, W. G. Chen, Y. L. Guo, Z. Y. Jiao, *J. Alloys Compd.* **2019**, *778*, 53.

[28] M. Han, K. Maleski, C. E. Shuck, Y. Yang, J. T. Glazar, A. C. Foucher, K. Hantanasirisakul, A. Sarycheva, N. C. Frey, S. J. May, V. B. Shenoy, E. A. Stach, Y. Gogotsi, *J. Am. Chem. Soc.* **2020**, *142*, 19110.

[29] J. Xiao, J. Wen, J. Zhao, X. Ma, H. Gao, X. Zhang, *Electrochim. Acta* **2020**, *337*, 135803.

[30] H. Ahmad, N. H. Abdul Kahar, R. Ramli, N. Yusoff, S. A. Reduan, M. F. Ismail, K. S. Lim, W. Y. Chong, M. Yasin, *Opt. Fiber Technol.* **2021**, *67*, 102683.

[31] M. Naguib, V. Presser, D. Tallman, J. Lu, L. Hultman, Y. Gogotsi, M. W. Barsoum, *J. Am. Ceram. Soc.* **2011**, *94*, 4556.

[32] C. J. Zhang, S. Pinilla, N. McEvoy, C. P. Cullen, B. Anasori, E. Long, S. H. Park, A. Seral-Ascaso, A. Shmeliov, D. Krishnan, C. Morant, X. Liu, G. S. Duesberg, Y. Gogotsi, V. Nicolosi, *Chem. Mater.* **2017**, *29*, 4848.

[33] X. Yang, Q. Wang, K. Zhu, K. Ye, G. Wang, D. Cao, J. Yan, *Adv. Funct. Mater.* **2021**, *31*, 1.

[34] K. Chen, Y. Guan, Y. Cong, H. Zhu, K. Li, J. Wu, Z. Dong, G. Yuan, Q. Zhang, X. Li, *J. Alloys Compd.* **2022**, *906*, 164302.

[35] P. Collini, S. Kota, A. D. Dillon, M. W. Barsoum, A. T. Fafarman, *J. Electrochem. Soc.* **2017**, *164*, 573.

[36] C. Zhang, L. Wang, W. Lei, Y. Wu, C. Li, M. A. Khan, Y. Ouyang, X. Jiao, H. Ye, S. Mutahir, Q. Hao, *Mater. Lett.* **2019**, *234*, 21.

[37] W. Zheng, P. Zhang, W. Tian, Y. Wang, Y. Zhang, J. Chen, Z. M. Sun, *Mater. Lett.* **2017**, *209*, 122.

[38] A. E. Allah, J. Wang, Y. V. Kaneti, T. Li, A. A. Farghali, M. H. Khedr, A. K. Nanjundan, B. Ding, H. Dou, X. Zhang, B. Yoshio, Y. Yamauchi, *Nano Energy* **2019**, *65*, 103991.

[39] M. Hu, Z. Li, H. Zhang, T. Hu, C. Zhang, Z. Wu, X. Wang, *Chem. Commun.* **2015**, *51*, 13531.

[40] T. Zhao, J. Zhang, Z. Du, Y. Liu, G. Zhou, J. Wang, *Electrochim. Acta* **2017**, *254*, 308.

[41] K. Li, X. Wang, X. Wang, M. Liang, V. Nicolosi, Y. Xu, Y. Gogotsi, *Nano Energy* **2020**, *75*, 104971.